Study of C/Doped δ-Bi$_2$O$_3$ Redox Reactions by in Operando Synchrotron X-ray Diffraction: Bond Energy/Oxygen Vacancy and Reaction Kinetics Relationships

Xizheng Wang, Rishvi Jayathilake, Daniel D. Taylor,[iD] Efrain E. Rodriguez,[iD] and Michael R. Zachariah*[iD]

University of Maryland, College Park, Maryland, 20740, United States

S *Supporting Information*

ABSTRACT: One major technical and economic hurdle on the sequestration of CO$_2$ is its separation from nitrogen when fossil fuels are burned in air. An alternative, thermodynamically equivalent approach is to use a metal oxide as an oxygen carrier (oxidizer) and then recycle the carrier following its reduction by exothermic reoxidation in air. This process, termed chemical looping combustion (CLC), places many requirements on the oxygen carrier. Here, we explore how to evaluate the relationship between the microscopic properties of an oxygen carrier and its performance in CLC. In this paper, systematically doped Bi$_2$O$_3$ were synthesized as oxygen carriers for the oxidation of carbon. In operando synchrotron X-ray diffraction and online mass spectrometry enable us to monitor both the phase evolution in the solid and the production of gaseous products. Initiation temperature and reaction kinetics were deduced on the basis of the X-ray diffraction peak intensity change. Results show that lower metal–oxygen bond energy and higher oxygen vacancy concentration of doped Bi$_2$O$_3$ led to lower onset temperature, faster reaction rate, and smaller activation energy for carbon oxidation. These results provide important insights into manipulating the atomic properties of oxygen carrier for CLC applications.
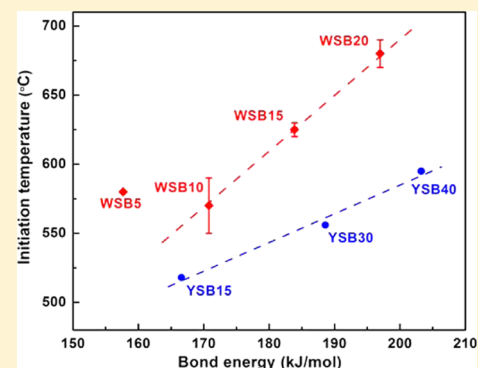
INTRODUCTION

The most convenient method to implement combustion is to use the oxygen in air, which nominally carries a thermal penalty of nitrogen. If one now considers sequestering CO$_2$, nitrogen poses an additional penalty during any subsequent separation process. One option is using pure oxygen, i.e., oxy-fuel combustion, which requires a preseparation process from air.[1−3]

Another approach that would mitigate the need for a nitrogen separation step is to employ an alternative source of oxygen. Notwithstanding water, which is the most abundant oxygen source but thermodynamically inaccessible as an oxidizer, metal oxides are ubiquitous oxygen carriers and, through judicious choice, can be used as oxidants to hydrocarbons or solid carbon. Naturally, such an approach only makes sense if the reduced oxide can be recycled and if thermodynamically there is little or no loss of overall energy efficiency per mass of fuel.

Chemical looping combustion (CLC) is an approach developed to employ metal oxides as oxygen carriers and to subsequently regenerate them by oxidation in air.[4,5] Because there is no net change in the oxygen carrier, thermodynamically this is equivalent to burning the fuel in air. The scientific challenge then becomes the exact choice of oxygen carrier and involves thermodynamic, kinetic, and material considerations as well as economics. Some important characteristics of a good oxygen carrier include its reactivity and stability in both reduction and oxidation cycles and its ability of completely combusting fuels. The latter character is important for the application to achieve maximum fuel combustion efficiency.

The central scientific question in choosing from an effective infinite variety of metal oxide combinations is how to choose, and more specifically, what makes for, a good oxygen carrier from a microscopy point of view. For obvious reasons, transition metal oxides have been the most widely studied and most focusing on exploring the reaction rate and cycling stability.[6,7] In studies where fuel is gaseous, the most studied simple oxygen carriers by now are Ni-based, Cu-based, and Fe-based transition oxides.[8,9] Some other studies focused on the direct oxygenation of carbon by those metal oxides. Siriwardane et al.[10] investigated coal CLC over CuO, Fe$_2$O$_3$, Co$_3$O$_4$, NiO, and Mn$_2$O$_3$ using thermogravimetric analysis and found that CuO showed the best reduction/oxidation performance. However, there are a large number of variables existing in those metal oxides that might impact CLC performance, including bond energy, oxygen mobility, crystal structure, reaction interface area, thermal conductivity, heat capacity, thermal contact, and so on. To deal with this complexity, a system is needed in which most of the dependent variables can be held constant. To improve the performance of condensed-phase CLC between carbon and metal oxide further, more must be known about the mechanism of the reaction.

A mixture of carbon and metal oxide is very similar to a thermite system with essentially the same type of redox reaction. Studies within our group have explored the reaction mechanism of C/CuO reaction by employing temperature-jump time-of-flight mass spectrometry (T-jump/TOFMS), and T-jump TOFMS measurements on C/CuO and bare CuO revealed the evidence of condensed-phase initiation of carbon oxidation by CuO.[11] In an earlier study, we employed a series of doped perovskites,[12] where crystal structure and morphology were removed as variables, for which we found a clear correlation between the measured initiation temperature and atomic properties of the oxidizer, such as metal–oxygen bond energy, oxygen vacancy concentration, and electronegativity. Another group of perovskites was selected as oxygen carriers for methane oxidation in CLC reactions, and the oxygen storage capacities of the perovskites were found to be dependent on the electronegativity of the transition metal on the B-site.[13] Another systematic metal oxide we studied was doped δ-Bi_2O_3, where we probed the oxygen-ion conductivity and found that we could correlate this to a threshold condition for reaction with solid fuel (Al, C, Ta).[14] Compared to that of perovskites, doped δ-Bi_2O_3 has higher oxygen mobility with ~25% of the oxygen sites vacant in its fluorite structure, and this is a reason why it is commonly employed as an electrolyte in solid-oxide fuel cells.[15,16] The high-conductivity δ-phase Bi_2O_3 is only high-temperature (730–824 °C) stable but can be stabilized down to room temperature by doping other metal ions.[17–19] Thus, in this study, we employ doped δ-Bi_2O_3 as oxygen carriers to study the structure–function relationship of oxygen carrier properties on carbon oxidation for CLC. We employ in operando synchrotron X-ray diffraction (SXRD) to study the trajectory of the reaction of carbon with yttrium and tungsten doped Bi_2O_3, synthesized by aerosol spray pyrolysis. Heating rates were varied to determine the activation energy for the carbon/doped Bi_2O_3 reaction. Our results show a very clear connection among oxygen vacancy concentration, average bond energy of oxygen carrier, and the initiation temperature, reaction rate, and activation energy of carbon/doped Bi_2O_3 redox reaction.

■ EXPERIMENTAL SECTION

Nanosized carbon black (~50 nm) was obtained from Cabot Corporation. $Bi(NO_3)_3 \cdot 5H_2O$ (≥98% pure) and $Y(NO_3)_3 \cdot 6H_2O$ (99.8% pure) were purchased from Sigma-Aldrich. $(NH_4)_6W_{12}O_{39} \cdot xH_2O$ was purchased from Alfa Aesar.

Synthesis of Doped Bi_2O_3. Seven doped Bi_2O_3, listed in Table 1, were synthesized by aerosol spray pyrolysis[20–22] at 750 °C with a residence time of about 1 s from metal nitrate contained aqueous solutions formulated with the desired metal ratios.

Table 1. Aerosol Spray Synthesized Doped Bi_2O_3

doped Bi_2O_3 formula	abbreviation
$(Y_{0.15}Bi_{0.85})_2O_3$	YSB15
$(Y_{0.3}Bi_{0.7})_2O_3$	YSB30
$(Y_{0.4}Bi_{0.6})_2O_3$	YSB40
$(W_{0.05}Bi_{0.95})_2O_{3.15}$	WSB5
$(W_{0.1}Bi_{0.9})_2O_{3.3}$	WSB10
$(W_{0.15}Bi_{0.85})_2O_{3.45}$	WSB15
$(W_{0.2}Bi_{0.8})_2O_{3.6}$	WSB20

To dissolve $Bi(NO_3)_3 \cdot 5H_2O$, 2 mol/L nitric acid was used. For example, to synthesize $(Y_{0.15}Bi_{0.85})_2O_3$, a 0.2 mol/L precursor solution, containing stoichiometric $Bi(NO_3)_3$ and $Y(NO_3)_3$, was atomized by a nebulizer to generate nominally 1 μm droplets with compressed air. The atomized droplets flowed through a diffusion dryer, where most of the water was absorbed and then the flow passed to a tubular furnace to produce the desired doped Bi_2O_3 particles. The final product was collected on a Millipore membrane with a pore size of 0.4 μm.

C/Bi_2O_3 Composites. Stoichiometric mixtures of carbon black particles and Bi_2O_3 were mixed and then sonicated in hexane for 30 min and dried in a hood overnight.

Material Characterization. The crystal structures of the as-synthesized Bi_2O_3 were characterized by X-ray diffraction (XRD) using a Bruker D8 diffractometer with Cu Kα radiation with an average wavelength of 1.54178 Å. Rietveld refinement of all diffraction patterns was performed with TOPAS 4.2 software.[23] The morphologies of the Bi_2O_3 were measured by scanning electron microscopy (SEM) with a Hitachi SU-70. Size distributions were obtained by measuring 300 individual nanoparticles statistically from SEM images of each sample, using Nano Measurer 1.2 image analysis software.

In Operando Synchrotron X-ray Powder Diffraction. In operando synchrotron powder X-ray diffraction (SXRD) experiments were performed in transmission mode on the 17-BM beamline at the Advanced Photon Source at Argonne National Laboratory. A two-dimensional PerkinElmer a-Si flat-panel detector was used with an average wavelength of 0.45336 Å, and diffraction images were integrated with GSAS-II,[24] giving patterns with a Q-range of approximately 0.2–6.2 Å^{-1}. A flow-cell/furnace sample holder[25] was used to control the sample temperature and atmosphere, and the measurement was under a gas flow of 100% He at 15 mL/min. Samples were diluted in fused quartz powder to minimize beam absorption.

To evaluate the redox reaction of C/doped Bi_2O_3, all of the samples were heated to 750 °C at 25 °C/min, with diffraction patterns collected every 30 s. For C/YSB, the samples were directly cooled down to room temperature after ramping with a cooling rate of ~100 °C/min. For C/WSB, after ramping, the samples were held at 750 °C for several minutes with diffraction patterns collected every 20 s and then cooled down to room temperature with diffraction patterns collected every 30 s. Peak refinement of all diffraction patterns was performed with sequential refinement modes of GSAS-II and TOPAS 4.2.

■ RESULTS AND DISCUSSION

All of the as-prepared doped Bi_2O_3 were synthesized by aerosol spray pyrolysis, and their XRD patterns and representative SEM image results are shown in Figures S1 and S2 and Table S1. On the basis of Rietveld refinements on the XRD patterns, all of the doped Bi_2O_3 have a single cubic phase in the $Fm\bar{3}m$ space group with the lattice parameters listed in Table 2. A previous published study aerosol sprayed doped Bi_2O_3 revealed that when synthesized under the same conditions (precursor concentration, follow rate, pyrolysis temperature, etc.), all samples share the same crystal structure, morphology, and size distribution.[14] All doped Bi_2O_3 in this study have an average particle size of about 90–100 nm with similar size distribution. With all of the doped Bi_2O_3 having similar crystal structure, particle size, and morphology, these factors can be considered eliminated as variables in carbon redox reaction. In our previous study, we estimated the metal–oxygen bond energy and oxygen

Table 2. Lattice Parameter, Percentage of Vacant Oxygen Sites in One Unit Cell, Oxygen Vacancy Concentration, and Metal−Oxygen (M−O) Bond Energy of Doped Bi₂O₃

doped Bi₂O₃	lattice parameters, a (Å)	percentage of vacant oxygen sites in one unit cell, r (%)	oxygen vacancy concentration, $[V_O^{\bullet\bullet}]$ (#/cm³)	M−O bond energy (kJ/mol)
WSB5	5.5985(3)	21.3	9.7×10^{-21}	158
WSB10	5.5945(2)	17.5	8.0×10^{-21}	171
WSB15	5.5915(4)	13.8	6.3×10^{-21}	184
WSB20	5.5565(5)	10	4.7×10^{-21}	197
YSB15	5.5230(3)	25	1.2×10^{-22}	167
YSB30	5.4895(8)	25	1.2×10^{-22}	189
YSB40	5.462(1)	25	1.2×10^{-22}	203

vacancy concentration, $[V_O^{\bullet\bullet}]$, based on the stoichiometry and thermodynamic parameters of doped Bi₂O₃.[14] We estimated the oxygen vacancy concentration, $[V_O^{\bullet\bullet}]$, based on the crystal structure of doped δ-Bi₂O₃. δ-Bi₂O₃ has a defect fluorite-type crystal structure (AX₂) in which 25% of the oxygen sites in the unit cell are vacant.[15] Y³⁺ has the same valence as Bi³⁺, so it is reasonable to assume that YSB also has ~25% vacant oxygen sites in the unit cell. We will show that Y³⁺ and W⁶⁺ substitute for Bi³⁺ at the same lattice site. However, W⁶⁺ has a higher

oxidation state,[26] so WO₃ should correspondingly have ~50% more oxygen than AX₂ in the oxygen sites. The percentage of vacant oxygen sites in one unit cell for each doped Bi₂O₃ is shown in Table 2. In one unit cell, 8 oxygen-ion sites exist. Oxygen vacancy concentrations of YSB and WSB can thus be estimated on the basis of the percentage of vacant oxygen sites in one unit cell and the lattice parameter. The calculated oxygen vacancy percentages in one unit cell and $[V_O^{\bullet\bullet}]$ of those doped Bi₂O₃ are shown in Table 2.

The metal−oxygen bond energies of these synthesized doped Bi₂O₃ were estimated on the basis of eq 1, where A stands for Bi, A′ is the dopant metal, and x is the dopant molar ratio. $\Delta(A−O)(\Delta(A′−O))$ represents the bond energy between $A(A′)$ cation and oxygen and is calculated by eq 2, where $\Delta H_{A_mO_n}$ is the heat of formation of A_mO_n at 298 K, ΔH_A is the heat of sublimation of A-metal at 298 K, and D_{O_2} is the dissociation energy of gaseous oxygen (498 kJ/mol).[27] The reader should recognize that eq 1 neglects any enthalpy of mixing of metal oxides. However, because we are interested in relative comparisons, we expect this to be a secondary effect. The calculated metal−oxygen bond energies of all doped Bi₂O₃ are listed in Table 2. The calculated bond energies increase with the dopant ratios of Y³⁺ and W⁶⁺ because the bond energies of
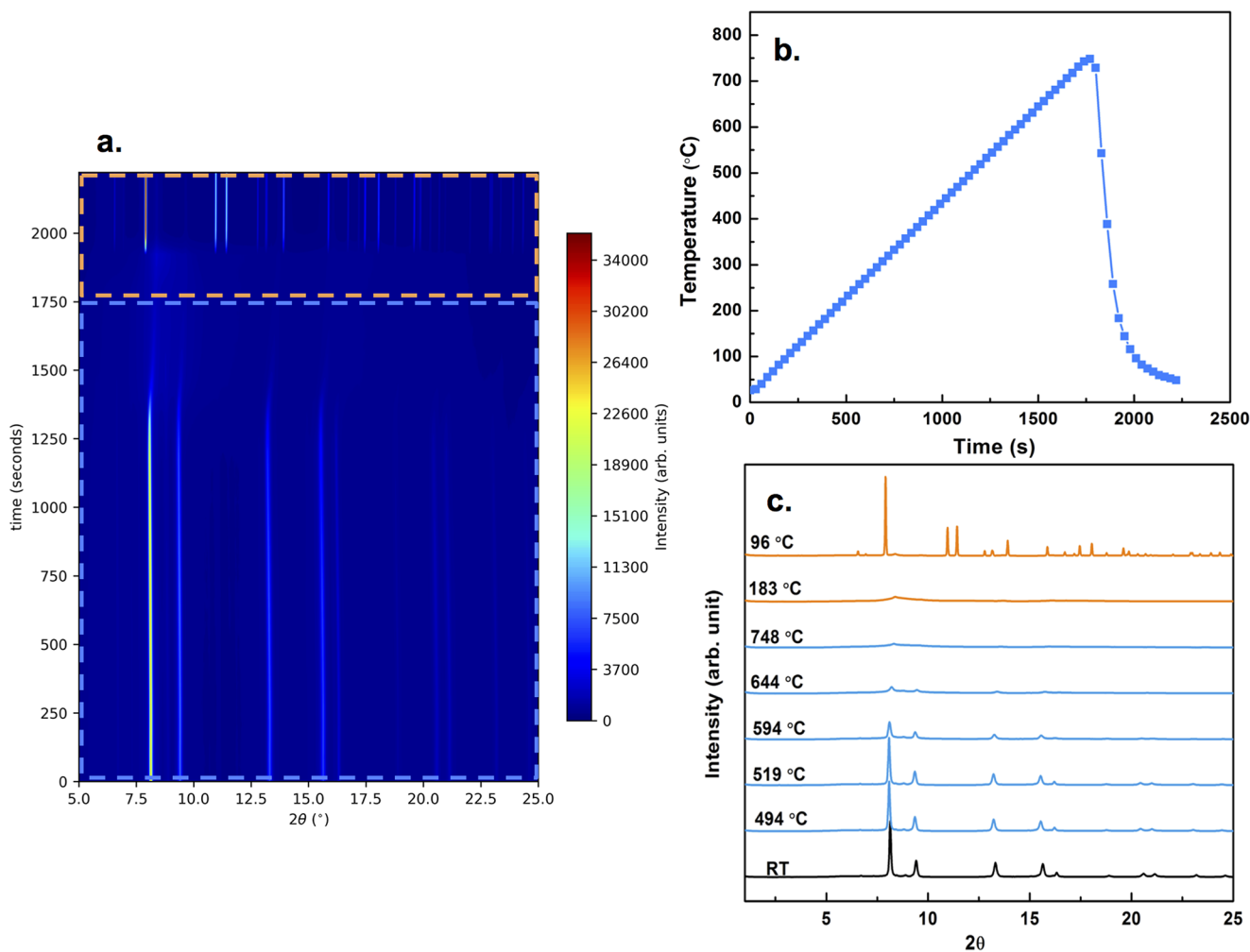
Figure 1. In operando SXRD (λ = 0.45336 Å) (a) contour plot, (b) temperature vs time, and (c) selected patterns for C/YSB15 at a heating rate of 25 °C/min, with the blue and orange boxes/curves representing heating and cooling, respectively.
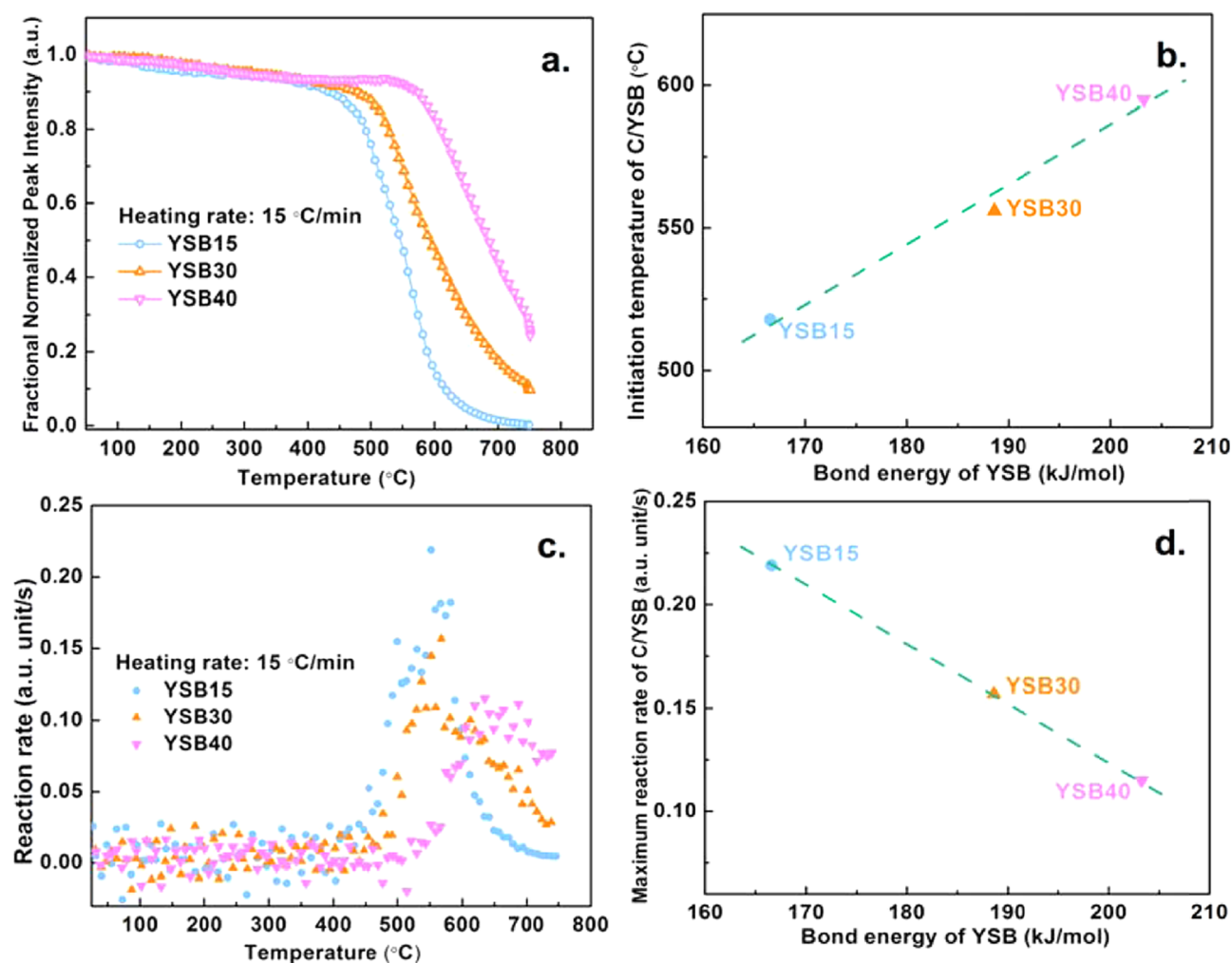
Figure 2. (a) Fractional normalized peak intensity for the (022) Bragg reflection ($2\theta \approx 13°$) and (c) instantaneous reaction rate for C with YSB15, 30, and 40 at a heating rate of 15 °C/min vs temperature. (b) Initiation temperature and (d) maximum reaction rate of C/YSB at a heating rate of 15 °C/min vs bond energy of YSB.

Y−O (~291 kJ/mol) and W−O (~406 kJ/mol) are larger than that of Bi−O (~145 kJ/mol).

$$\text{M−O bond energy} = (1 - x)\cdot\Delta(\text{A−O}) + x\cdot\Delta(\text{A'−O}) \tag{1}$$

$$\Delta(\text{A−O}) = \frac{1}{6m}\left(\Delta H_{\text{A}_m\text{O}_n} - m\Delta H_\text{A} - \frac{n}{2}D_{\text{O}_2}\right) \tag{2}$$

In Operando Reaction of Carbon with Yttrium Doped Bi$_2$O$_3$. Figure 1a shows a contour plot of SXRD patterns (74 scans) of C/YSB15 at all recorded temperatures at a heating rate of 25 °C/min, with the blue and orange boxes representing heating and cooling, respectively. Figure 1b shows the temporal temperature profile, indicating a ramping process with a constant heating rate and a rapid cooling process. Figure 1c shows representative SXRD patterns of C/YSB15 (selected eight scans) at selected temperatures, with the blue and orange curves representing heating and cooling, respectively. In the SXRD patterns, the δ-phase of Bi$_2$O$_3$ dominates the diffraction pattern because carbon black is amorphous. Crystallizing in a cubic structure with space group $Fm\overline{3}m$, δ-Bi$_2$O$_3$ has an anion-deficient fluorite-type structure where the oxide vacancies are disordered.[28] Representative Rietveld refinements for cubic YSB15 are shown in Figure S3a, with structure information

listed in Table S2. These results confirmed that Y^{3+} and Bi^{3+} share the same positions in the lattice and that only a single phase exists. As the temperature increased, the peak intensity of C/YSB15 decreased and was almost gone by ~650 °C. We regarded the peak intensity decay as the indication of consumption of YSB15 and thus the completion of the oxidation reaction. The redox reaction of C/YSB15 occurs on the order of minutes, necessitating diagnostics such as SXRD, which can collect complete diffraction patterns every 30 s during the reaction. Because Bi would be molten at these high temperatures, not until the reactor was cooled below ~200 °C did we observe the crystallization of elemental Bi. Representative refinement for Bi in rhombohedral $R\overline{3}m$ is shown in Figure S3b.

Reaction Energetics. In our previous study of thermite composites of doped Bi$_2$O$_3$ with aluminum at a high heating rate, we found that ignition temperature (reaction threshold) increased with the metal−oxygen bond energy of doped Bi$_2$O$_3$ (oxidizer).[14] A mixture of carbon and doped Bi$_2$O$_3$ is physically similar to a mixture of aluminum and doped Bi$_2$O$_3$ and may share reaction energetic properties. YSB15, 30, and 40, with the same $[V_\text{O}^{\bullet\bullet}]$, were used as the oxygen carriers to explore the effect of metal−oxygen bond energy on carbon redox initiation temperature. As stated above, the decays of SXRD peaks were
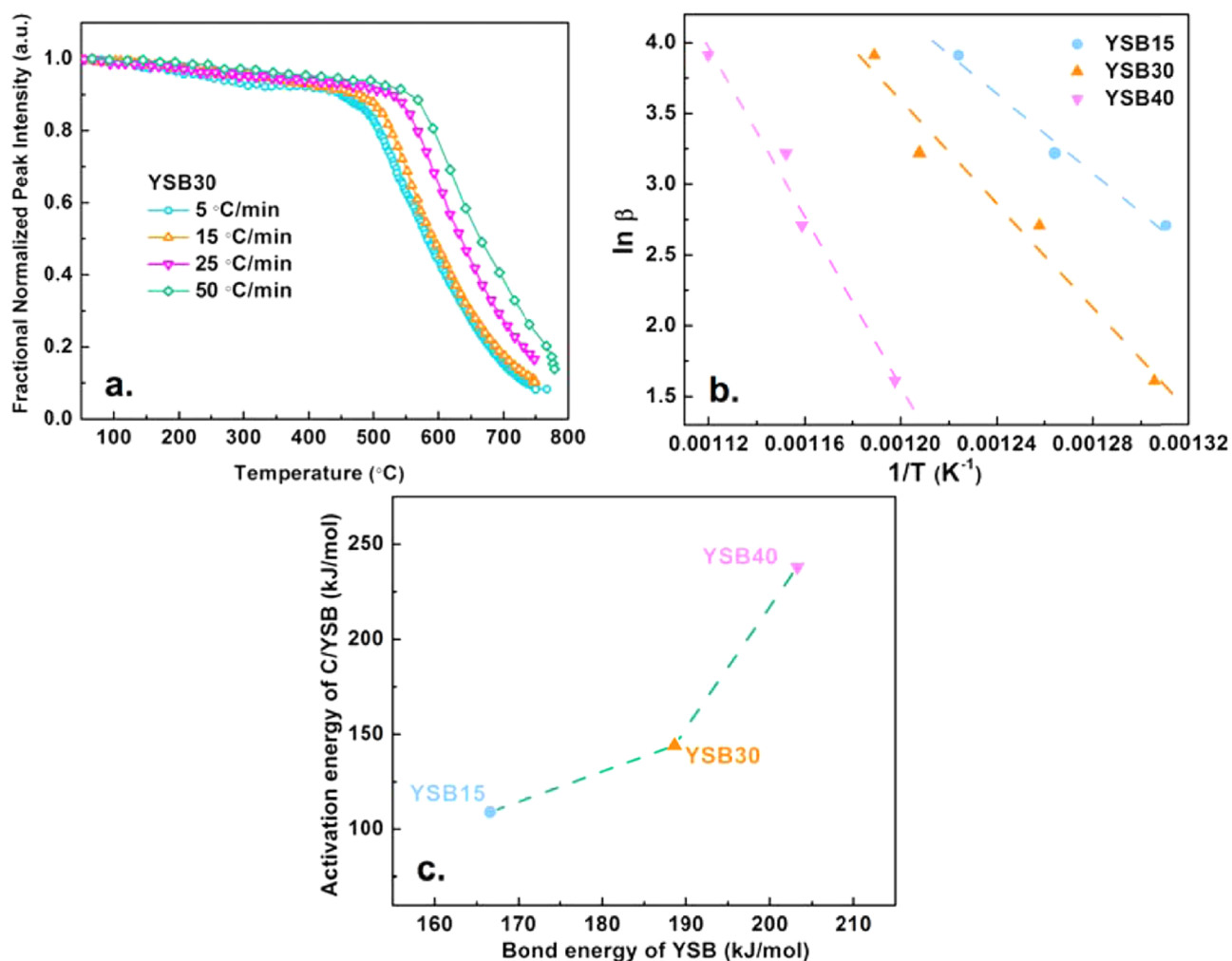
Figure 3. a) Fractional normalized peak intensity for the (022) Bragg reflection ($2\theta \approx 13°$) of YSB30 mixed with carbon at variable heating rates: 5, 15, 25, and 50 °C/min vs temperature. (b) Arrhenius plots for the Ozawa isoconversion method. (c) Activation energy of C/YSB vs bond energy of YSB.

regarded as the occurrence of redox reaction. To determine the initiation temperature, single peak fits to the (022) Bragg reflection located at $2\theta \approx 13°$ were performed using the sequential refinement mode of GSAS-II. Fractional normalized peak intensity vs temperature for YSB15, 30, and 40 at a heating rate of 15 °C/min is shown is Figure 2a. We found that the peak intensity stayed near-constant in time and then had a sharp drop off that was linear. We thus make a tangent to the linear drop-off region and extrapolate until it intersects the near-horizontal peak intensity initially seen. This intersection is the onset of reaction. An illustration of initiation temperature determination is shown is Figure S4. These initiation temperatures show a clear increase with higher M−O bond energy in Figure 2b. The reaction rate can be evaluated by mapping the temperature (*x*-axis) to time, through the heating rate, and then taking the instantaneous slope of Figure S5. The calculated instantaneous reaction rate vs temperature is shown in Figure 2c. C/YSB15 had the highest peak reaction rate and initiates at a lower temperature, whereas C/YSB40 had the lowest peak reaction rate, which occurred at a higher temperature. This is also consistent with a simple observation of Figure 2a; the extent of reaction at 750 °C shows a faster overall rate in the order YSB15 > YSB30 > YSB40. Plotting the peak reaction rate seen in Figure 2c with respect to M−O bond energy also shows that the peak reaction rate observed scales with bond energy (Figure 2d). Lower M−O bond energy leads to earlier and faster reaction.

Activation Energy vs Bond Energy. A variable heating rate (5, 15, 25, and 50 °C/min) experiment was also performed to determine the apparent activation energy for the initiation reaction of C/YSB. Fractional normalized peak intensity vs temperature for carbon with YSB at a heating rate of 25 °C/min is shown in Figure S6. Figure 3a shows the representative fractional normalized peak intensity vs temperature for C/YSB30 at different heating rates. We used the same method as above to determine the initiation temperatures.

In this study, we employ the Flynn−Wall−Ozawa isoconversion method[29−32] to calculate the apparent activation energy for the reaction initiation. This isoconversion method is based on the principle that the reaction rate at a constant extent of conversion is a function only of temperature, which allows for model-free estimates of the activation energy. No assumption on reaction order is needed. We have already studied in our prior paper that the reaction between solid carbon and solid doped Bi_2O_3 is condensed-phase reaction without the revolution of O_2 because doped Bi_2O_3 is stable without decomposition when heated up to its melting point.[14] The Osawa method[30,32] employs eq 3, where β is the heating

rate, T is the initiation temperature, and E_a is the activation energy for the initiation reaction to determine the apparent activation energy. The results are shown in Figure 3b, with activation energy determined from the slope of the Arrhenius plot.

$$\ln \beta = \text{constant} - \frac{1.052 E_a}{RT} \tag{3}$$

The calculated activation energies for the initiation of C/YSB15, 30, and 40 are 109, 144, and 238 kJ/mol, respectively, which are also plotted in Figure 3c, showing again a correlation that high M−O bond energy increases the activation energy for reaction. Although not a one-for-one comparison, the magnitudes of the bond energy and activation energies are remarkably similar and are reminiscent of what one observes for simple bond fission processes.

CO$_2$ Release from the Redox Reaction. CO_2 was reported to be the main product specie of carbon combustion.[33] The release of gaseous products, CO_2 and CO, was in situ analyzed by a residual gas analyzer coupled with SXRD. Figure 4 shows the temporal CO_2 and CO
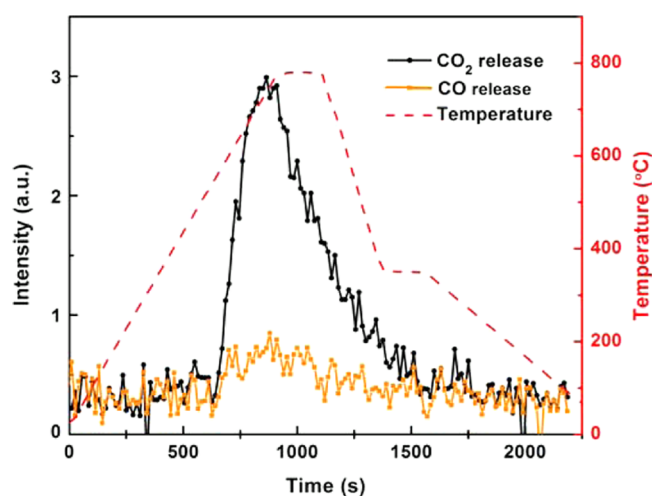
Figure 4. Temporal temperature and CO_2 and CO/N_2 release from C/YSB30 at a heating rate of 50 °C/min.

concentrations for C/YSB30 at a heating rate of 50 °C/min along with the temperature profile. The appearance of CO_2 at ~570 °C closely coincides with the initiation temperature determined from the SXRD peak decay. CO, on the contrary, is only slightly above background, indicating that the combustion was complete with little likely coke formation.

Carbon with Tungsten Doped Bi$_2$O$_3$. Compared with C/YSB composites, we found the reaction in the C/WSB system to be more complex. Although WSB synthesized in this study was stable at room temperature in the cubic δ-Bi$_2$O$_3$ form, it was unstable upon heating. Figure 5a shows a contour plot of the SXRD patterns of C/WSB20 at a heating rate of 25 °C/min. Figure 5b shows the temporal temperature profile, indicating a ramping-up process, a steady-state region, followed by a cooling process. Figure 5c shows eight representative SXRD patterns at selected temperatures. Compared to that of C/YSB, C/WSB20 displays a more complex change during heating. As the temperature increased, we see a shift to higher angles, indicating a decrease in unit cell volume. This transition occurs between 570 and 610 °C and is highlighted for the reader by the green box denoting the boundaries. After the

peak shift, no change in peak intensity is observed until ~680 °C, indicating that we are observing peak shifts resulting from thermal effects and not reaction with carbon. Reaction commences at ~680 °C, and the XRD effectively showed little crystal structure by 750 °C. The small peaks at 750 °C were analyzed by the peak match shown in Figure S7. A broad bump was found in the 2θ range of 5−12, which we believe belongs to unreacted amorphous carbon and amorphous/liquid bismuth. The other peaks could possibly be assigned to WO_2, WO_3, and Bi_4O_7, indicating the partial activity of W^{6+} with carbon. Similar to the case in C/YSB, when cooled, Bragg reflections corresponding to Bi do not appear until the temperature was cooled down below ~200 °C, as seen in the SXRD patterns in the orange box/curves shown in Figure 5a,c.

Contour plots of SXRD patterns and representative SXRD patterns of C/WSB5, C/WSB10, and C/WSB15 at selected temperatures are shown in Figures S8−S10. Similar observations of peak movements from lower angle to higher angle within the cubic structure were found for all WSB samples when heated above ~580 (±20) °C. However, for C/WSB5, we also observed a phase change from cubic to monoclinic when heated to ~400 °C and a phase change back to cubic from monoclinic when heated above ~580 °C. A more detailed analysis can be found in the Supporting Information. In situ XRD of WSB5 (Figure S12) shows that even in the absence of carbon, we observe the phase change from cubic to monoclinic but not monoclinic back to cubic. Thus, we can conclude that phase change from cubic to monoclinic is due to thermal effects, whereas phase change from monoclinic back to cubic is due to the interaction with carbon.

Initiation Temperature Relationship of Bond Energy and Oxygen Vacancy Concentration. For C/YSB, initiation temperatures were determined on the basis of the peak intensity profile. However, different from C/YSB, whose peak intensity decay was only due to the consumption of YSB, the peak intensity change of C/WSB was more complex. The phase changes between cubic and monoclinic and peak movements to higher angle might also lead to peak intensity changes. Because the 2θ ≈ 8° (single peak (111) for cubic and (132) for monoclinic) sustained a single peak over the whole reaction for C/WSB, we focused on it as the signature for subsequent refinement using TOPAS 4.2. For all samples, in the peak shift range, peak intensities of peaks that are very close at 2θ ≈ 8.0° and 8.2° that occurred at higher temperature ($T > 600$ °C) were added together. Fractional normalized peak intensity vs temperature for carbon with WSB5, 10, 15, and 20 at a heating rate of 25 °C/min is shown in Figure S13. Initiation temperatures are defined on the basis of the peak intensity change with temperature and are listed in Table S4, with detailed description shown in the Supporting Information.

The correlation of initiation temperature of C/doped Bi$_2$O$_3$ with metal−oxygen energy of doped Bi$_2$O$_3$ at a heating rate of 25 °C/min is shown in Figure 6. It is apparent that, similar to the C/YSB results, the initiation temperature of C/WSB increased with metal−oxygen bond energy of doped Bi$_2$O$_3$. The initiation temperature of C/WSB5 did not follow the C/WSB trend, which is probably due to the reduced oxygen-ion mobility of WSB5 resulting from the phase change from the vacancy-abundant cubic to vacancy-lean monoclinic structure.[34] It is also noted that C/WSB and C/YSB have different trends of initiation temperature vs bond energy. This is also likely due to the reduced oxygen vacancy concentration of WSB compared to that of YSB. For example, WSB15 has similar
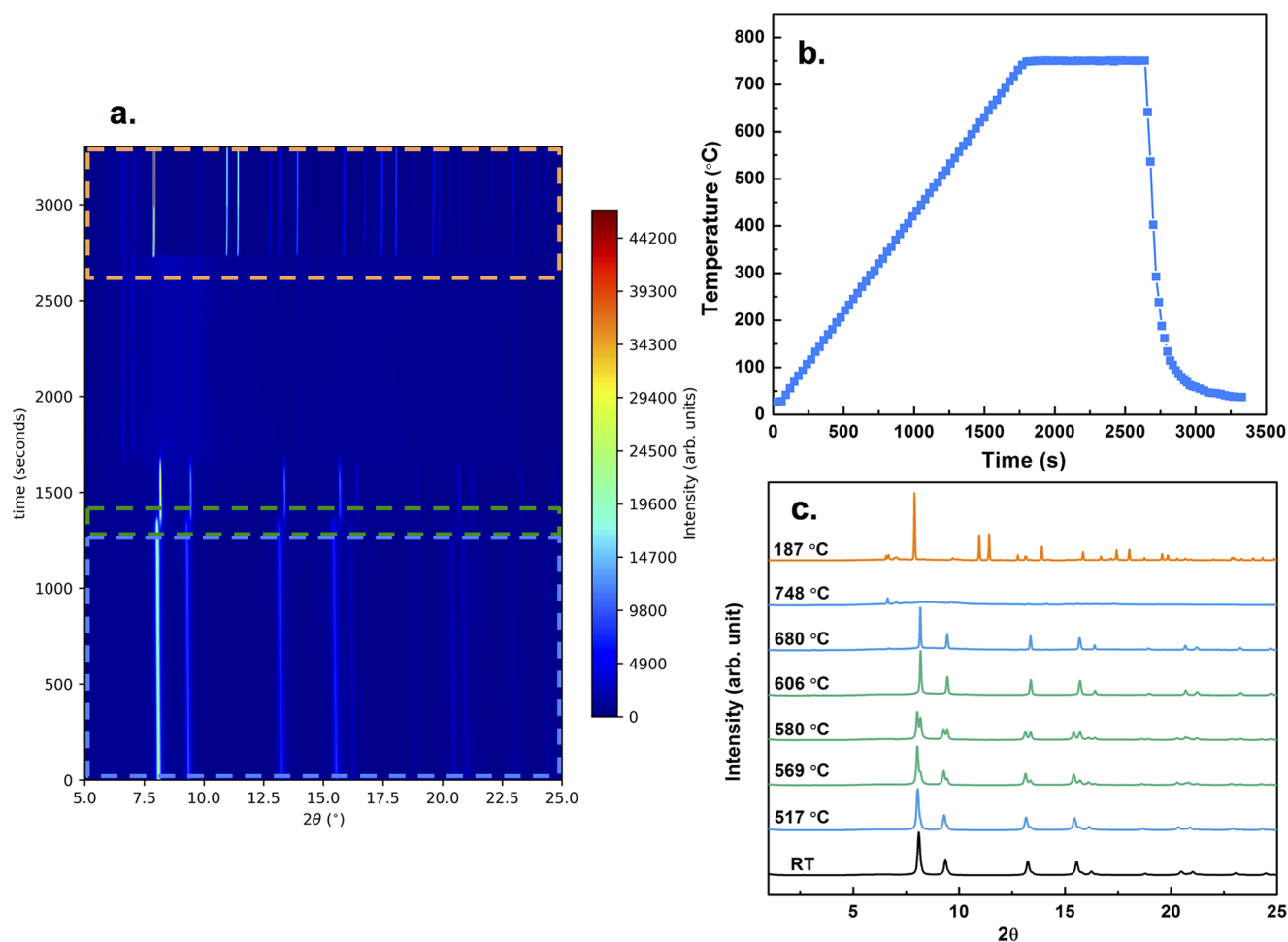
Figure 5. In operando SXRD (λ = 0.45336 Å) (a) contour plot, (b) temperature vs time, and (c) selected patterns for C/WSB20 at a heating rate of 25 °C/min, with the blue box/curves of WSB20 in cubic structure, green showing peak shifts within cubic structure, and orange in the cooling process.
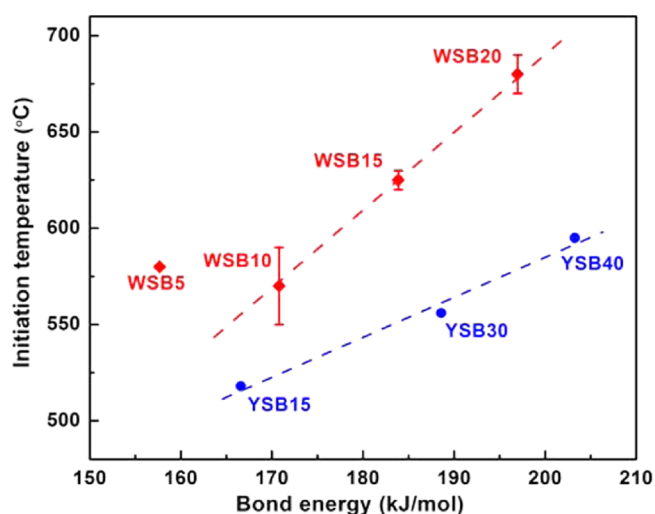
Figure 6. Initiation temperature of C/doped Bi_2O_3 vs bond energy of doped Bi_2O_3.

metal−oxygen bond energy as YSB30, but C/WSB15 reacted at a higher temperature than C/YSB30, which may be due to YSB30 having a larger oxygen vacancy concentration. Thus, we conclude that oxygen vacancy also affects the initiation

temperature, similar to our previous observation of the oxidation on metals.[12,14]

CONCLUSIONS

In this paper, systematically doped Bi_2O_3 were employed to better understand how the properties of an oxygen carrier influence the oxidation of carbon for CLC applications. In operando synchrotron X-ray diffraction and online mass spectrometry were used to monitor both the phase evolution in the solid and the production of gaseous products. Initiation temperature and reaction kinetics were extracted to show that lower metal−oxygen bond energy and higher oxygen vacancy concentration of doped Bi_2O_3 led to lower onset temperature, faster reaction rate, and smaller activation energy for carbon oxidation. These results provide important insights into manipulating oxygen carrier's atomic properties for CLC applications.

ASSOCIATED CONTENT

S **Supporting Information**

The Supporting Information is available free of charge on the ACS Publications website at DOI: 10.1021/acs.jpcc.8b01402.

XRD, representative SEM, and particle size distribution for doped Bi_2O_3; representative XRD patterns fitted on the basis of Rietveld refinement for YSB15 in $Fm\overline{3}m$,

bismuth in $R\bar{3}m$, and WSB5 in $Fm\bar{3}m$ and $I12/m\ 1$; initiation temperature define for C/doped Bi_2O_3; in operando SXRD contour plot and selected patterns for C/WSB5, 10, and 15; in situ XRD for WSB5 (PDF)

■ AUTHOR INFORMATION

Corresponding Author
*E-mail: mrz@umd.edu.

ORCID
Daniel D. Taylor: 0000-0003-1862-3946
Efrain E. Rodriguez: 0000-0001-6044-1543
Michael R. Zachariah: 0000-0002-4115-3324

Notes
The authors declare no competing financial interest.

■ ACKNOWLEDGMENTS

■ REFERENCES

(1) Coombe, H. S.; Nieh, S. Polymer Membrane Air Separation Performance for Portable Oxygen Enriched Combustion Applications. *Energy Convers. Manage.* **2007**, *48*, 1499−1505.

(2) Baukal, C. E., Jr.; Gershtein, V. Y.; Heffron, J. F.; Best, R. C.; Eleazer, P. B. Method and Apparatus for Reducing NO_x Production During Air-Oxygen-Fuel Combustion. U.S. Patent 5,871,343, 1999.

(3) Liang, M. S.; Kang, W. K.; Xie, K. C. Comparison of Reduction Behavior of Fe_2O_3, ZnO and $ZnFe_2O_4$ by TPR Technique. *J. Nat. Gas Chem.* **2009**, *18*, 110−113.

(4) Richter, H. J.; Knoche, K. F. Reversibility of Combustion Processes. *ACS Symp. Ser.* **1983**, *235*, 71−85.

(5) Adánez, J.; de Diego, L. F.; García-Labiano, F.; Gayán, P.; Abad, A. Selection of Oxygen Carriers for Chemical-Looping Combustion. *Energy Fuels* **2004**, *18*, 371−377.

(6) Liu, L.; Wu, Y.; Hu, J.; Liu, D.; Zachariah, M. R. Zeolite-Supported Iron Oxides as Durable and Selective Oxygen Carriers for Chemical Looping Combustio. *Energy Fuels* **2017**, *31*, 11225−11233.

(7) Luo, S.; Zeng, L.; Fan, L. S. Chemical Looping Technology: Oxygen Carrier Characteristics. *Annu. Rev. Chem. Biomol. Eng.* **2015**, *6*, 53−75.

(8) Hossain, M. M.; de Lasa, H. I. Chemical-Looping Combustion (CLC) for Inherent CO_2 Separations—A Review. *Chem. Eng. Sci.* **2008**, *63*, 4433−4451.

(9) Nandy, A.; Loha, C.; Gu, S.; Sarkar, P.; Karmakar, M. K.; Chatterjee, P. K. Present Status and Overview of Chemical Looping Combustion Technology. *Renewable Sustainable Energy Rev.* **2016**, *59*, 597−619.

(10) Siriwardane, R.; Tian, H.; Richards, G.; Simonyi, T.; Poston, J. Chemical-Looping Combustion of Coal with Metal Oxide Oxygen Carriers. *Energy Fuels* **2009**, *23*, 3885−3892.

(11) Piekiel, N. W.; Egan, G. C.; Sullivan, K. T.; Zachariah, M. R. Evidence for the Predominance of Condensed Phase Reaction in Chemical Looping Reactions Between Carbon and Oxygen Carriers. *J. Phys. Chem. C* **2012**, *116*, 24496−24502.

(12) Wang, X.; Wu, T.; Zachariah, M. R. Doped Perovskites to Evaluate the Relationship Between Fuel-Oxidizer Thermite Ignition and Bond Energy, Electronegativity and Oxygen Vacancy. *J. Phys. Chem. C* **2017**, *121*, 147−152.

(13) Liu, L.; Taylor, D. D.; Rodriguez, E. E.; Zachariah, M. R. Influence of Transition Metal Electronegativity on the Oxygen Storage Capacity of Perovskite Oxides. *Chem. Commun.* **2016**, *52*, 10369−10372.

(14) Wang, X.; Zhou, W.; DeLisio, J.; Egan, G.; Zachariah, M. R. Doped δ-Bismuth Oxides to Investigate Oxygen Ion Transport as a Metric for Condensed Phase Thermite Ignition. *Phys. Chem. Chem. Phys.* **2017**, *19*, 12749−12758.

(15) Harwig, H. A. On the Structure of Bismuthsesquioxide: The α, β, γ, and δ-Phase. *Z. Anorg. Allg. Chem.* **1978**, *444*, 151−166.

(16) Jacobson, A. J. Materials for Solid Oxide Fuel Cells. *Chem. Mater.* **2010**, *22*, 660−674.

(17) Jung, D. W.; Duncan, K.; Wachsman, E. D. Doubly Doped Bi_2O_3 Electrolytes With Higher Conductivity. *ECS Trans.* **2006**, *1*, 63−71.

(18) Takahashi, T.; Iwahara, H. High Oxide Ion Conduction in Sintered Oxides of the System Bi_2O_3-WO_3. *J. Appl. Electrochem.* **1973**, *3*, 65−72.

(19) Wachsman, E. D.; Lee, K. T. Lowering the Temperature of Solid Oxide Fuel Cells. *Science* **2011**, *334*, 935−939.

(20) Wu, T.; SyBing, A.; Wang, X.; Zachariah, M. R. Aerosol Synthesis of Phase Pure Iodine/Iodic Biocide Microparticles. *J. Mater. Res.* **2017**, *32*, 890−896.

(21) Jian, G.; Liu, L.; Zachariah, M. R. Facile Aerosol Route to Hollow CuO Spheres and Its Superior Performance as An Oxidizer in Nanoenergetic Gas Generators. *Adv. Funct. Mater.* **2013**, *23*, 1341−1346.

(22) Yang, Y.; Romano, M.; Feng, G.; Wang, X.; Wu, T.; Holdren, S.; Zachariah, M. R. Growth of sub-5 nm Metal Nanoclusters in Polymer Melt Aerosol Droplets. *Langmuir* **2018**, *34*, 585−594.

(23) Cheary, R. W.; Coelho, A. A. Fundamental Parameters Approach to X-Ray Line-Profile Fitting. *J. Appl. Crystallogr.* **1992**, *25*, 109−121.

(24) Toby, B. H.; Von Dreele, R. B. GSAS-II: The Genesis of a Modern Open-Source All Purpose Crystallography Software Package. *J. Appl. Crystallogr.* **2013**, *46*, 544−549.

(25) Chupas, P. J.; Chapman, K. W.; Kurtz, C.; Hanson, J. C.; Lee, P. L.; Grey, C. P. A Versatile Sample-Environment Cell for Non-Ambient X-Ray Scattering Experiments. *J. Appl. Crystallogr.* **2008**, *41*, 822−824.

(26) Borowska-Centkowska, A.; Krok, F.; Abrahams, I.; Wrobel, W.; Dygas, J. R.; Hull, S. Thermal Variation of Structure and Electrical Conductivity in $Bi_{14}WO_{24}$. *Solid State Ionics* **2011**, *202*, 14−21.

(27) Lide, D. R. Standard Thermodynamic Properties of Chemical Substances. *CRC Handbook of Chemistry and Physics*; CRC Press, 2007; Vol. 5.

(28) Hull, S.; Norber, S. T.; Tucker, M. G.; Eriksoon, S. G.; Mohn, C. E.; Stolen, S. Neutron Total Scattering Study of the δ and β Phases of Bi_2O_3. *Dalton Trans.* **2009**, 8737−8745.

(29) Flynn, J. H.; Wall, L. A. General Treatment of the Thermogravimetry of Polymers. *J. Res. Natl. Bur. Stand.* **1966**, *70A*, 487−523.

(30) Jian, G.; Zhou, L.; Piekiel, N. W.; Zachariah, M. R. Low Effective Activation Energies for Oxygen Release from Metal Oxides: Evidence for Mass-Transfer Limits at High Heating Rates. *ChemPhysChem* **2014**, *15*, 1666−1672.

(31) Vyazovkin, S.; Burnham, A. K.; Criado, J. M.; Perez-Maqueda, L. A.; Popescu, C.; Sbirrazzuoli, N. ICTAC Kinetics Committee Recommendations for Performing Kinetic Computations on Thermal Analysis Data. *Thermochim. Acta* **2011**, *520*, 1−19.

(32) Zhou, W.; DeLisio, J. B.; Wang, X.; Egan, G. C.; Zachariah, M. R. Evaluating Free vs Bound Oxygen on Ignition of Nano-Aluminum Based Energetics Leads to a Critical Reaction Rate Criterion. *J. Appl. Phys.* **2015**, *118*, No. 114303.

(33) Wu, T.; Wang, X.; DeLisio, J. B.; Holdren, S.; Zachariah, M. R. Carbon Addition Lowers Initiation and Iodine Release Temperatures from Iodine Oxide-Based Biocidal Energetic Materials. *Carbon* **2018**, *130*, 410−415.

(34) Sammes, N. M.; Tompsett, G. A.; Näfe, H.; Aldinera, F. Bismuth Based Oxide Electrolytes-Structure and Ionic Conductivity. *J. Eur. Ceram. Soc.* **1999**, *19*, 1801−1826.